Second International Symposium on Marine Propulsors
smp'11, Hamburg, Germany, June 2011
Workshop: Propeller performance

Cavitation Simulations of the Potsdam Propeller Test Case

Sergey Yakubov, Bahaddin Cankurt, Thierry Maquil, Patrick Schiller, Moustafa Abdel-Maksoud, Thomas Rung

Institute of Fluid Dynamics and Ship Theory, Hamburg University of Technology (TUHH), Hamburg, Germany

ABSTRACT

The paper presents results for the cavitation simulations of the Potsdam Propeller Test Case (i.e. test cases 2.3.x of the SMP'11 Workshop). Three requested cases at different cavitation numbers and thrust coefficients are computed using the in-house viscous simulation procedure FreSCo$^+$. All simulations were performed using an URANS approach with a $k-\omega$ turbulence model. Cavitating-flow results are mostly obtained from a traditional VOF-based Euler-Euler approach to capture the two-phase flow phenomena. Examples included reveal, that such approaches should be used carefully, as results may strongly depend on applied model parameters. Accordingly, a more sophisticated Euler-Lagrange approach to cavitation modeling is presented and some preliminary results are shown.

Keywords

Propeller-flow simulations, Cavitation models, Euler-Euler, Euler-Lagrange.

1 INTRODUCTION

Cavitation is known as the formation and subsequent rapid collapse of vapor bubbles inside liquid streams. The process is primarily governed by the deviation of the liquid pressure from the vapour pressure. In marine applications, cavitation has various undesirable effects on propellers and rudders, such as pressure-fluctuation induced noise and vibration, erosion and performance deterioration.

Typically, a VOF-based Euler-Euler approach which considers the flow as a dynamic liquid/vapour mixture is used for simulations of cavitating marine-engineering flows. The two componentes of the mixture share the same velocity field which is described by the Navier-Stokes equations. The local vapour-volume fraction is computed from an additional transport equation. The latter employs a source term, describing the mass transfer between the liquid and the vapor phase derived from a simplified Rayleigh-Plesset equation.

The Euler-Euler concept allows two-way coupling between liquid and vapor phase and may be quite efficient for some flows. Since it doesn't take into account inhomogeneous water properties and is restricted to simplified dynamics at no slip between vapour-bubbles and liquid, it often requires questionable, case-dependent calibration of model parameters.

Another approach to cavitation modelling refers to the Euler-Lagrange approach. Here the vapour-volume fraction is obtained by simulating the evolution of individual bubbles, composing a discrete phase (Abdel-Maksoud et al., 2010). The dynamics of these bubbles is computed using Newtonian equations of motion coupled with the Rayleigh-Plesset equation for the description of the bubble size. As such approach considers each bubble individually, it allows to take into account various forces, acting on the bubble, as well as bubble-boundary interactions, slip-flow effects and inhomogeneous or transient water quality aspects, i.e. bubbles spectra of the approach flow and the local non-condensable gas content.

In this paper cavitating propeller flow was studied for the Potsdam Propeller Test Case (PPTC) in the framework of the Second International Symposium on Marine Propulsors (SMP'11) workshop. In addition to the required data submitted for validation, here we present more details on specific issues such as grid resolution influence, model parameters study, noncavitating/cavitation flows comparison and some preliminary results for the Euler-Lagrange approach.

2 NUMERICAL METHOD

2.1 FreSCo+

FreSCo$^+$ is a spin-off of FreSCo, a joint development of Hamburg University of Technology (TUHH), Hamburgische Schiffbau-Versuchsanstalt (HSVA) and Maritime Research Institute Netherlands (MARIN) (Rung et al., 2009). The original code was developed within the scope of the EU initiative VIRTUE. The procedure uses a segregated algorithm based on the strong conservation form of the momentum equations. It employs a cell-centered, co-located storage arrangement for all transport properties. Structured and unstructured grids, based on arbitrary polyhedral cells or hanging nodes, can be used.

The implicit numerical approximation is second-order accurate in space and time. Integrals are approximated using the conventional mid-point rule. The solution is iterated to convergence using a pressure-correction SIMPLE scheme. Various turbulence-closure models are available with respect to statistical (RANS) or scale-resolving (LES, DES) approaches.

Since the data structure is generally unstructured, suitable pre-conditioned iterative sparse-matrix solvers for symmetric and non-symmetric systems (e.g. GMRES, BiCG,

QMR, CGS or BiCGStab) can be employed. The algorithm is parallelised using a domain-decomposition technique based on a Single Program Multiple Data (SPMD) message-passing model, i.e. each process runs the same program on its own subset of data. Inter-processor communication employs the MPI communications protocol. Load balancing is achieved using the ParMETIS partitioning software.

Cavitation is modelled using either mass-transfer models (Euler-Euler) or two-way coupled Euler-Lagrange approaches.

2.2 Govering equations

The fluid mixture of an incompressible liquid and bubbles containing vapour and homogeneous gas is described by the standard Navier-Stokes equations under the assumption of isothermal state:

$$\frac{\partial \rho}{\partial t} + \nabla \cdot (\rho \mathbf{u}) = 0 \tag{1}$$

$$\frac{\partial \rho \mathbf{u}}{\partial t} + (\mathbf{u} \cdot \nabla)(\rho \mathbf{u}) = -\nabla p + \nabla \boldsymbol{\tau}, \tag{2}$$

where $\boldsymbol{\tau}$ is the viscous stress tensor with components

$$\tau_{ij} = \mu \left(\frac{\partial u_i}{\partial x_j} + \frac{\partial u_j}{\partial x_i} - \frac{2}{3}\delta_{ij}\frac{\partial u_k}{\partial x_k} \right).$$

The mixture density ρ and mixture viscosity μ are computed as a sum of partial densities and viscosities of the fluid (l) and vapour (v):

$$\begin{aligned} \rho &= \alpha \rho_v + (1-\alpha)\rho_l \\ \mu &= \alpha \mu_v + (1-\alpha)\mu_l \end{aligned} \tag{3}$$

Here α is the vapour-volume fraction defined as the ratio between the vapor volume and the total volume of a control volume

$$\alpha = \frac{V_v}{V_v + V_l}\ . \tag{4}$$

A control volume (CV) filled with fluid yields $\alpha = 0.0$, a control volume filled with vapor $\alpha = 1.0$, respectively. For $\alpha \in]0.0, 1.0[$ the CV is filled with a mixture of fluid and vapor. Values out of this range describe non-realisable situations.

Euler-Euler and Euler-Lagrange approaches to α-computations are described below.

Within **Euler-Euler** approach, the vapour-volume fraction is computed from a transport equation with a source term S_{cav}:

$$\frac{\partial \alpha}{\partial t} + \nabla(\alpha \mathbf{u}) = S_{\text{cav}} \tag{5}$$

The source term can be approximated via several empriri-cal models. The present work employs the model reported by Zwart(Zwart et al., 2004)

$$S_{\text{cav}} = \begin{cases} F_{\text{vap}} \cdot \frac{3\ \alpha_{\text{nuc}}}{R_0} \cdot \sqrt{\frac{2}{3}\frac{|p_v - p|}{\rho_l}}(1-\alpha), p_v < p \\ F_{\text{cond}} \cdot \frac{3}{R_0} \cdot \sqrt{\frac{2}{3}\frac{|p_v - p|}{\rho_l}}\alpha, p_v > p \end{cases}\ . \tag{6}$$

The Zwart model inheres two empirical constants F_{vap} and F_{cond} which allow to distinguish between vaporisation and condensation. Two additional model paramters are the initial nucleation-site volume fraction α_{nuc} and the corresponding initial nucleation-site radius R_0. Mind that these parameters are assigned to constant values and do not vary in space or time.

Within **Euler-Lagrange** approach vapour-volume fraction is defined by mapping bubbles on the Eulerian mixture field. The local vapour volume in a cell is computed as a sum of volumes of individual bubbles, residing in this cell. An interpolation procedure is applied to get smooth field which is limited within physical bounds.

Considering a bubble as a small rigid sphere, its trajectory can be described by the equation of motion (Maxey and Riley, 1983; Oweis, 2005; Abdel-Maksoud et al., 2010):

$$\begin{aligned} \frac{d\mathbf{x}}{dt} = \mathbf{v};\ \ m_b \frac{d\mathbf{v}}{dt} &= (m_b - m_f)\mathbf{g} + m_f \frac{D\mathbf{u}}{Dt} - \\ &- \frac{1}{2} m_f \left(\frac{d\mathbf{v}}{dt} - \frac{D\mathbf{u}}{Dt} \right) + \mathbf{F}_D + \mathbf{F}_L + \mathbf{F}_V \end{aligned} \tag{7}$$

where m_b is the bubble mass, m_f is the equivalent mass of the carrier phase, $\mathbf{v}$ - bubble velocity, $\mathbf{u}$ - carrier phase velocity at the center of the bubble. The first three terms on the right-hand side of (7) are the forces due to buoyancy, fluid acceleration and added mass (inertia). $\mathbf{F}_D, \mathbf{F}_L, \mathbf{F}_V$ denote to the drag, lift, and volume variation forces.

While the equation of motion (7) provides the bubble's trajectory, the Rayleigh-Plesset equation – including a term accounting for the effect of the slip velocity between the bubble and the carrier phase – determines the time-varying radius of the bubble (Hsiao et al., 2000):

$$R\ddot{R} + \frac{3}{2}\dot{R}^2 = \frac{1}{\rho_f}\left[p_v + p_g - p_\infty - \frac{2\sigma}{R} - \frac{4\mu_f}{R}\dot{R} \right] + \frac{(\mathbf{u} - \mathbf{v})^2}{4} \tag{8}$$

3 COMPUTATIONAL SET-UP

3.1 Propeller Geometry and computational domain

A five-blade controllable pitch propeller is proposed for the workshop. The propeller diameter refers to D=250mm. It features a chord length at r/R=0.7 of c/D= 0.417, a pitch ratio at r/R=0.7 of 1.635, a hub diameter ratio of 0.3, an area ratio of 0.779 and skew angle of 18.8°. For the simplicity of mesh generation the gap between hub and propeller is closed.

The whole 5-blade propeller is embedded in a cylindrical domain. The radius of the domain denotes 1.34 D, providing the same cross-sectional area size as the experiment. The computational domain covers 2D upstream of the propeller and 4D in downstream direction.

3.2 Computational mesh

Two non-conformal body-fitted fully hexahedral unstructured meshes have been generated using NUMECA HEXPRESS™software. The first mesh contains $4.7 \cdot 10^6$ cells.

It utilizes local refinement in the tip vortex region (hollow cylinder) and downstream the hub (Figure 1). In order to assess the blade resolution dependency, one of the blades is refined better than the others. The grid is built for the use with wall functions with $y^+ \approx 60$.

The second mesh features locally refined cells at the location of the tip vortex. In order to reduce mesh size this refinement was applied only for one blade. Figure 2 shows the refinement area. The typical cell dimension in this region is 0.5x0.5x0.5 mm. The total size of the second grid is $9.4 \cdot 10^6$ cells.

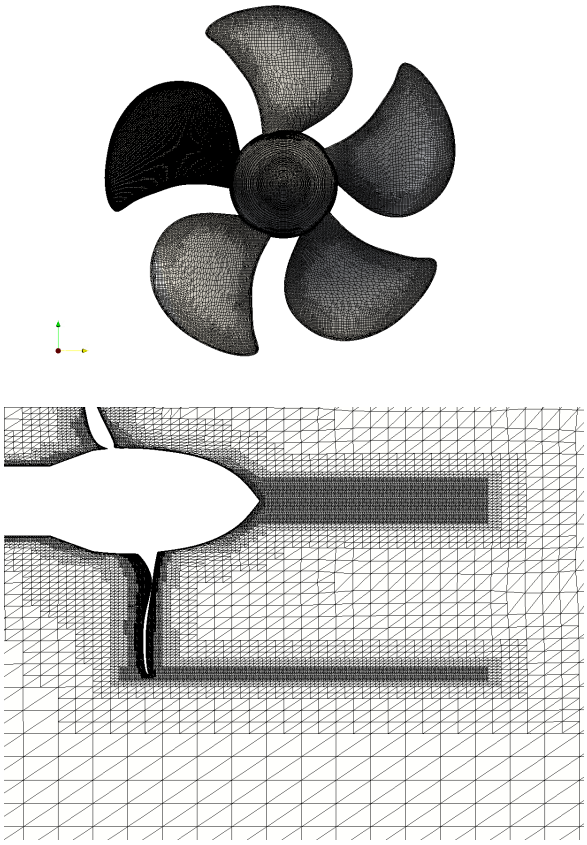

Figure 1: $4.7 \cdot 10^6$ cells mesh

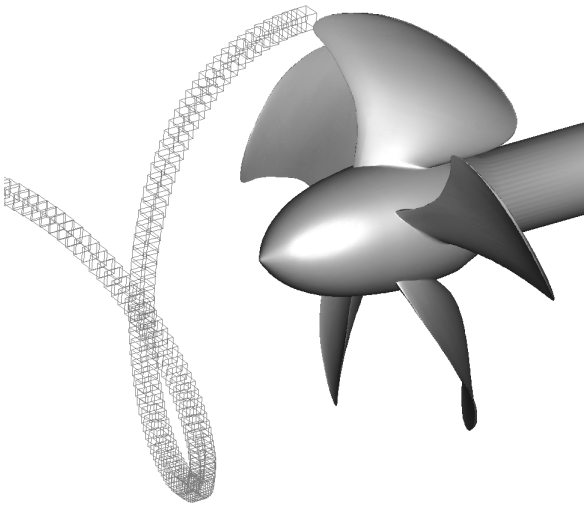

Figure 2: $9.4 \cdot 10^6$ cells mesh. Refinement region

3.3 Numerical settings

For all computed cases unsteady RANS simulations with the Wilcox $k-\omega$ turbulence model (Wilcox, 2004) have been performed. The QUICK convection scheme without limitations is used for all transport properties. The time step corresponded to 1°of the propeller rotation and the resulting Courant number is $Co < 1$. The simulations are performed in an inertial frame of reference. Computational domain is rotating at a given revolution rate.

As already outlined before, the Zwart model is used to describe the liquid/vapour mass transfer. The empirical coefficients are assigned to the literature-reported values of Zwart (Zwart et al., 2004). Initial nuclei parameters follow from $\alpha_{nuc} = 1.\ 10^{-6}$ and $R_0 = 5 \cdot 10^{-4}$ m. Notice that the values for F_{vap} and F_{cond} were deliberately varied for the simulations.

In general, three propeller revolutions were required to obtain stable results. Cavitating cases started from non-cavitating results after one propeller revolution.

3.4 Boundary contitions

A uniform velocity was used at the inflow boundary. The value was adjusted so that non-cavitating propeller have the same thrust coefficient as in the experiments. Table 1 presents inlet velocity values used in simulations.

Table 1: Inlet velocities

Case	V_{inlet} measured [m/s]	V_{inlet} adjusted [m/s]
2.3.1	6.37	6.6
2.3.2	7.93	8.1
2.3.3	8.8	9.03

At the outlet boundary a uniform pressure was specified matching the given cavitation number for each case. No-slip walls with wall functions were set at the hub and propeller blades. A slip-wall boundary condition was employed along the outer circumference.

4 RESULTS

4.1 Tip vortex resolution

Using the mesh of $4.7 \cdot 10^6$ cells shown in Figure 1, no cavitation was observed for all of the cases in the tip vortex region. The resolved vortex is not strong enough to cause the required pressure reduction in it's core which would initiate the onset of cavitation. Therefore, the initial mesh has been modified by refining the tip vortex region for one blade and another mesh of $9.4 \cdot 10^6$ cells has been generated. Figure 3 shows comparisons of vorticity iso-surfaces obtained with both grids. As depicted by the figure the tip vortex is resolved much better for the finer mesh. As illustrated in Figure 4, cavitation is now seen near the blade featuring the refined tip-vortex region.

Tip-vortex cavitation itself has a limited influence on the propeller performance, but in some cases it is a starting point for the sheet cavitation on the blade. Thus it may be important to be able to resolve this kind of cavitation.

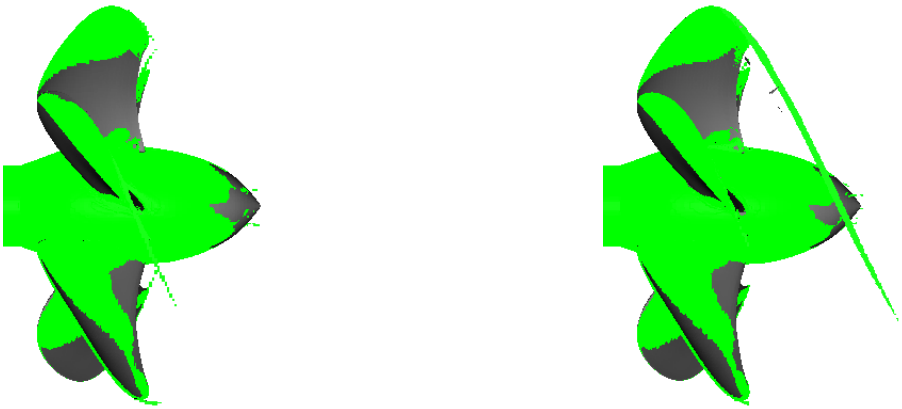

Figure 3: Case 2.3.1. VorticityX = 1000 isosurfaces. $4.7 \cdot 10^6$ (left) and $9.4 \cdot 10^6$ (right) cells meshes

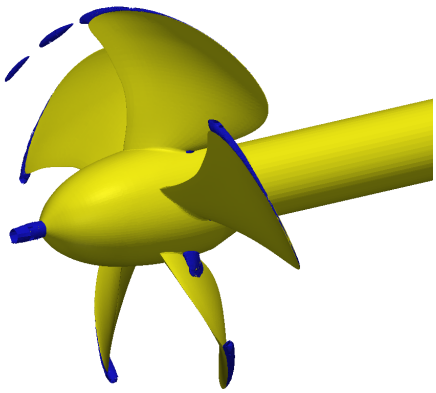

Figure 4: Case 2.3.1. $C_{cav} = 0.2$ isosurface for $9.4 \cdot 10^6$ cells mesh

4.2 Comparisons of non-cavitating and cavitating results

Figures 5 and 6 show comparisons between corresponding results for non-cavitating and cavitating simulations. One can observe that cavitation occurs in regions with pressure below vapor pressure for the non-cavitating case (see Figure 7). The pressure in this regions gets closer to vapor pressure for the cavitating case, i.e. pressure increases in the latter case. It can be also seen that shear stresses are reduced during the cavitation process which might be related to local changes in mixture properties in cavitation regions.

4.3 Cavitation model parameter influence

The originally suggested in (Zwart et al., 2004) parameters in the expression for the vaporisation/condensation source term (6) are F_{vap}=50, F_{cond}=0.01. From our previous experience with 2D foils cavitation simulations, results may be quite sensitive to the choise of the model parameters.

A parameter study has been performed to investigate the respective coefficient influence of F_{vap} and F_{cond} for case 2.3.2. Three different parameters sets as displayed in Table 3 were used. Mind that they are well within the range of recommended values. The table reveals, that the computed thrust coefficients differ substantially from the non-cavitating case – from 50% reduction for high values to virtually no changes for small values – depending on the choice of coefficients. The result can be attributed to different predictions of the cavitation volume, which is clearly seen from Figures 8, 9 and 10.

In case of high parameter values, an excessive vapor volume is produced in the propeller regime. It displaces the primary flow and is convected over a large portion of the domain downstream of the propeller which is of course unphysical (but the solution is converged). In conjunction with smaller values cavitation exist only in regions near the propeller hub and tip and with the smallest values cavitation region gets very small.

This study shows that Euler-Euler cavitation models may reqiure case-dependend calibration of constants which might be inappropriable for industrial uses. The conclusion applies not only to the employed Zwart model but also any other mass-transfer model of this type.

Table 2: Zwart model (Zwart et al., 2004) parameter study

$F_{\text{vap}}/F_{\text{cond}}$	K_{T}
25/0.005	0.137
5/0.005	0.211
0.1/0.001	0.242
non-cavitating measurements	0.245

4.4 Euler-Lagrange model results

Initial simulations of for case 2.3.1 have been performed with the Euler-Lagrange model. A specified number of nu-

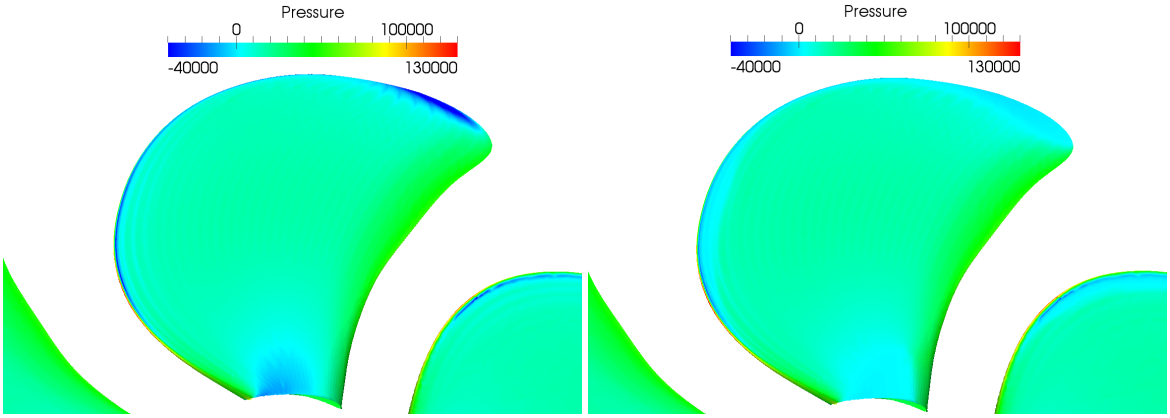

Figure 5: Case 2.3.1. Suction side pressure field, $9.4 \cdot 10^6$ cells mesh. Non-cavitating (left) and cavitating (right) propeller

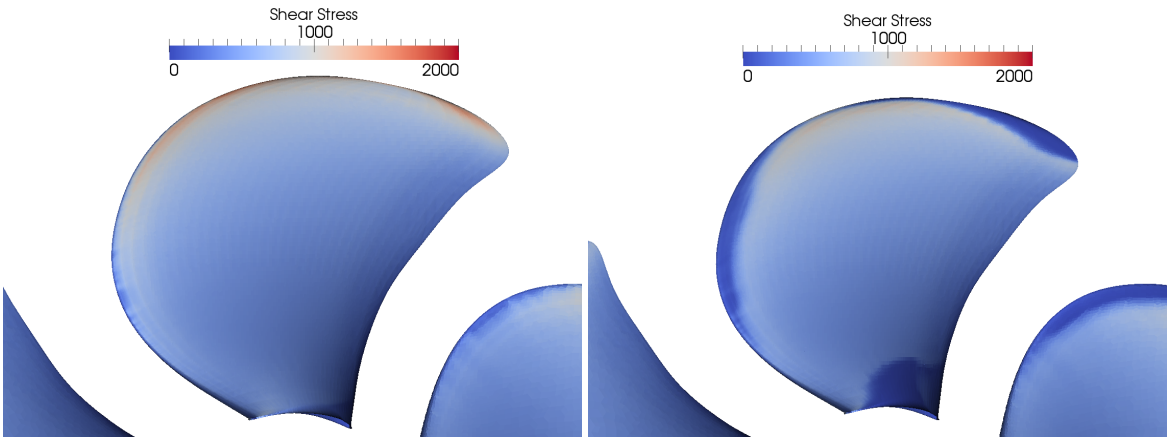

Figure 6: Case 2.3.1. Shear stresses on the suction side. $9.4 \cdot 10^6$ cells mesh. Non-cavitating (left) and cavitating (right) propeller

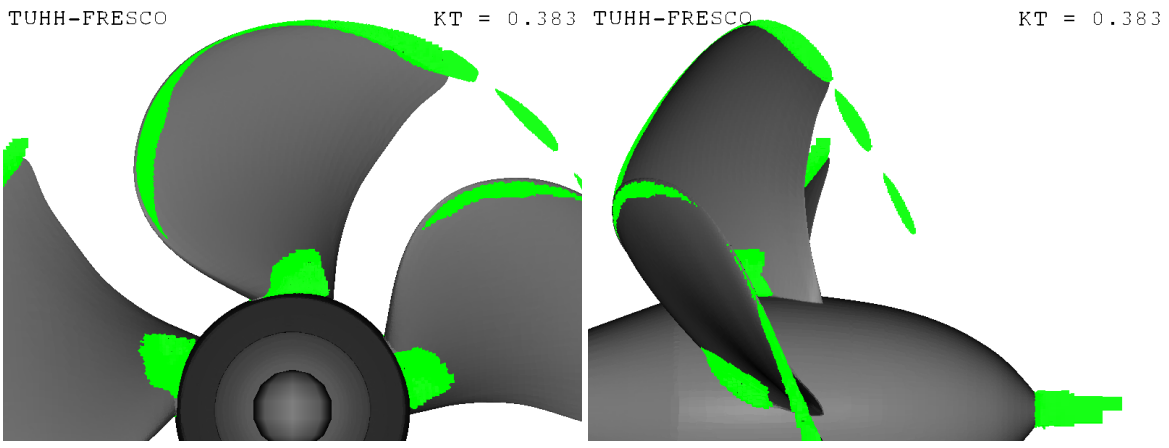

Figure 7: Case 2.3.1. $C_{cav} = 0.2$ isosurface for $9.4 \cdot 10^6$ cells mesh

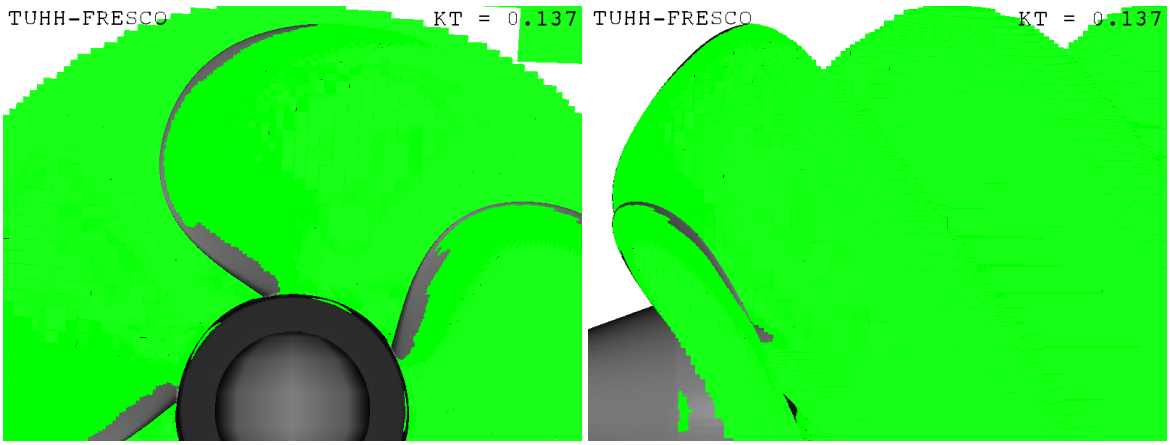

Figure 8: Case 2.3.2. $C_{cav} = 0.2$ isosurface for $4.7 \cdot 10^6$ cells mesh. F_{vap}=25, $F_{\text{cond}} = 0.005$

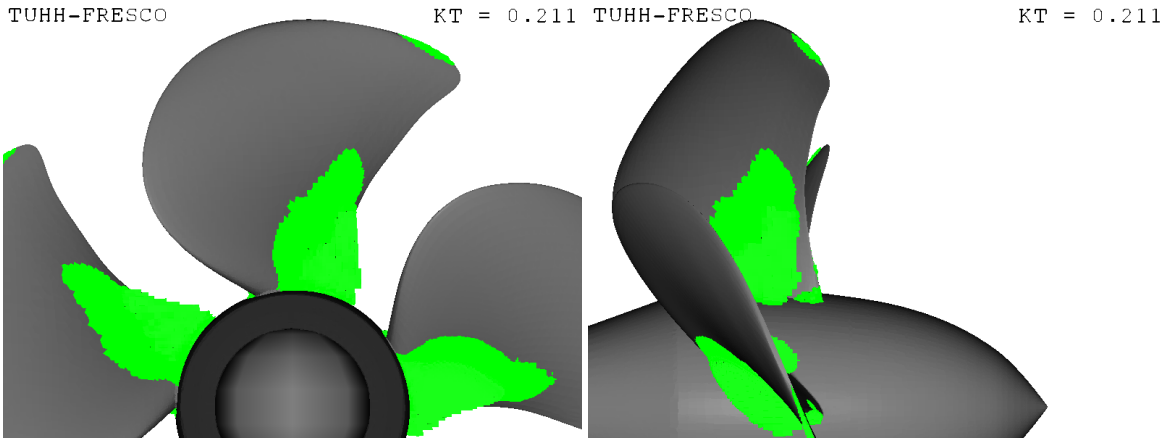

Figure 9: Case 2.3.2. $C_{cav} = 0.2$ isosurface for $4.7 \cdot 10^6$ cells mesh. F_{vap}=5, $F_{\text{cond}} = 0.005$

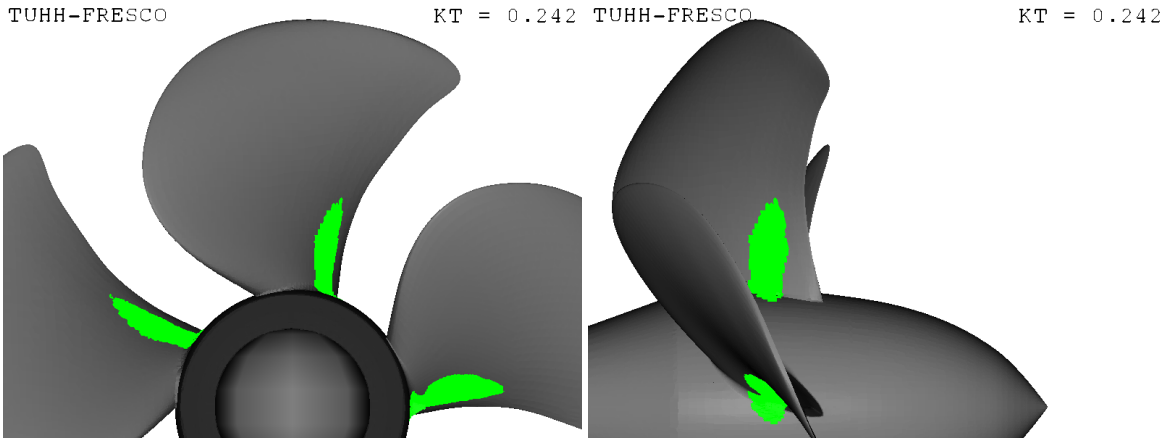

Figure 10: Case 2.3.2. $C_{cav} = 0.2$ isosurface for $4.7 \cdot 10^6$ cells mesh- F_{vap}=0.1, $F_{\text{cond}} = 0.001$

clei (100 bubbles of 100 micron diameter) are started each Eulerian time step at a given position upstream the propeller. Ideally, the initial bubble distribution should depend on the water quality and flow conditions, but at first steps it is chosen arbitrary here. The starting position is chosen such that injected bubbles could get into the low pressure tip region. To consider sheet cavitation near the hub, more bubbles must be started upstream the propeller.

When a bubble travels through the low-pressure region, it starts to grow accordingly to the Rayleigh-Plesset equation (8). Figure 11 displays a bubble distribution in the tip region. Some cavitation already occurs in the tip vortex, although for this mesh Euler-Euler model revealed no cavitation.

It should be mentioned, that simulation with Euler-Lagrange model are quite time-consuming. The study was supported by high-performance computing hardware and required the introduction of hybrid MPI/OpenMP parallelisation strategies.

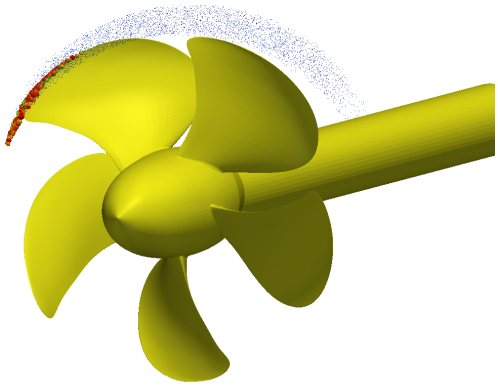

Figure 11: Euler-Lagrange simulations. $4.7 \cdot 10^6$ cells Euler mesh, 10000 bubbles

4.5 Open-water tests

In addition to cavitating cases, open water curve has case been computed. Another mesh of $4 \cdot 10^6$ cells similar to the coarser mesh for cavitating simulations was generating taking into account different hub geometry (Figure 12) and domain size (with raduis of four propeller diameters D, 4D upstream of the propeller and 10D in downstream direction). The computed data is given in Table. Figure 13 shows the open-water diagramm.

Table 3: Open-water test case results

J	K_T	$10K_Q$	η_0
0.6	0.612	1.407	0.415
0.8	0.501	1.203	0.530
1.0	0.393	0.999	0.626
1.2	0.279	0.780	0.683
1.4	0.168	0.561	0.667

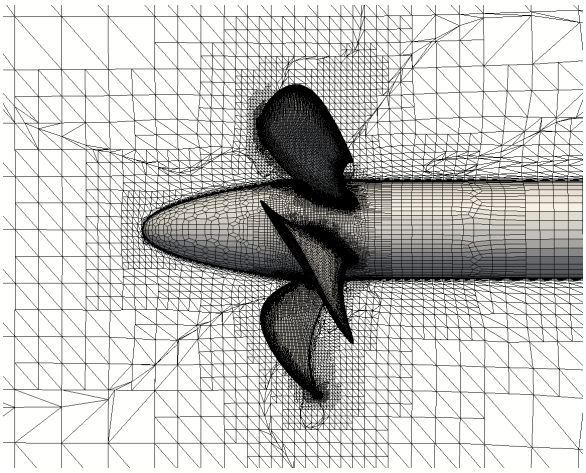

Figure 12: $4 \cdot 10^6$ cells mesh used for open-water simulations

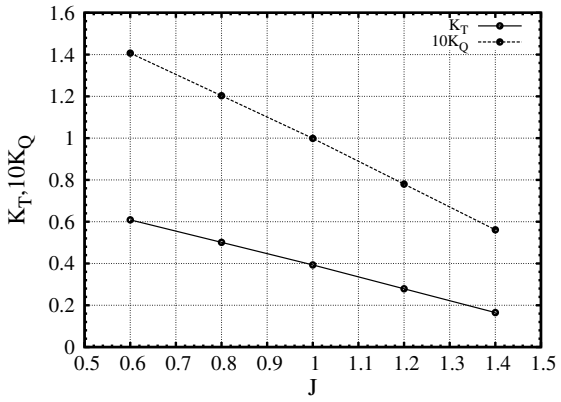

Figure 13: Open-water diagramm

CONCLUSIONS

Results for the cavitation and open-water simulations of the Potsdam Propeller Test Case (test cases 2.1 and 2.3 of the SMP'11 Workshop) are presented in the paper. It is shown that to correctly resolve tip vortex cavitation quite fine mesh is required in this region. Cavitation results obtained by the Euler-Euler model show significant dependency on it's internal constants. An alternative, Euler-Lagrange approach is suggested and some preliminary results are shown. Further work on sheet cavitation simulations with Euler-Lagrange model is planned.

ACKNOWLEDGMENTS

The current work is a part of the research project funded by German Ministery of Economics and Technology (BMWi; Grant Nr. 3SX286A) in the framework of the "Schifffahrt und Meerestechnik für das 21. Jahrhundert" research initiative. The simulations were performed on the HLRN-II supercomputer system at the North German Cooperation for High-Performance computing (HLRN). This support is gratefully acknowledged by the authors.

REFERENCES

M. Abdel-Maksoud, D. Hänel, and U. Lantermann. Modeling and computation of cavitation in vortical flow. *Int. J. of Heat and Fluid Flow*, 31(6):1065 – 1074, 2010.

C.-T. Hsiao, G. L. Chahine, and H.-L. Liu. Scaling effect on bubble dynamics in a tip vortex flow: Prediction of cavitation inception and noise. Technical report, Dynaflow, Inc., 2000.

M. R. Maxey and J. R. Riley. Equation of motion for a small rigid sphere in a nonuniform flow. *J. Physics of Fluids*, 26(4):883–889, April 1983.

G.F. Oweis. Capture and inception of bubbles near line vortices. *J. Physics of Fluids*, 17:022105, 2005.

T. Rung, K. Wöckner, M. Manzke, J. Brunswig, C. Ulrich, and A. Stück. Challenges and Perspectives for Maritime CFD Applications. *Jahrbuch der Schiffbautechnischen Gesellschaft, 103. Band*, 2009.

D.C. Wilcox. *Turbulence Modeling for CFD*. DCW Industries, Inc., 2 edition, 2004.

P.J. Zwart, A.G. Gerber, and T. Belamri. A two phase flow model for predicting cavitation dynamics. In *ICMF 2004 International Conference on Multiphase Flow*, 2004. Yokohama, Japan, May 30 – June 3, 2004.